Supporting Information

Ion Gel Dynamic Templates for Large Modulation of Morphology and Charge Transport Properties of Solution-Coated Conjugated Polymer Thin Films

Erfan Mohammadi[1], Chuankai Zhao[1], Fengjiao Zhang[1]†, Ge Qu[1], Seok-Heon Jung[2], Qiujie Zhao[3], Christopher M. Evans[3], Jin-Kyun Lee[2], Diwakar Shukla[1], and Ying Diao[1*]

[1]Department of Chemical and Biomolecular Engineering, University of Illinois at Urbana−Champaign, Urbana, Illinois 61801, United States.

[2]Department of Polymer Science & Engineering, Inha University, Incheon 402-751, South Korea.

[3]Department of Materials Science and Engineering, University of Illinois at Urbana−Champaign, Urbana, Illinois 61801, United States.

*E-mail: yingdiao@illinois.edu

Supplementary Methods

Molecular Dynamics (MD) Simulations and Analysis

All the MD simulations were performed with the AMBER18 MD software package[1] on the Blue Waters petascale computing facility. In all cases, the MD simulations were carried out following standard protocols. Specifically, beginning with an initial random configuration generated using the Packmol[2], we then subjected the system to a long equilibration prior to the data collection. In all cases, the force field parameters were derived from the general AMBER force field (GAFF)[3]. All the partial charges were derived using the AM1/BCC method as implemented in the AMBERTools14[1]. A previous study has reported that the GAFF is able to accurately predict IL transport and thermodynamic properties[4]. Periodic boundary conditions were employed in all the simulations with an integration time step of 2 fs. Particle-mesh Ewald method[5] was used to treat electrostatic interactions with a 10 Å cut-off distance. The SHAKE algorithm[6] was applied to constrain the length of covalent bonds involving hydrogen atoms to their equilibrium values. Berendsen thermostat and barostat[7] were used to maintain the system temperature and pressure (for simulations in constant pressure ensemble only). More details of the simulation parameters for each specific set of simulations are described below.

1. Ion gel interfacial properties

We performed extensive all atom MD simulations to compare ion gel surface properties under vacuum and upon exposure to chloroform. Based on our XPS results, the ion gel template with 80 wt% pre-gel solution IL contains 55 wt% IL in the top surface (Figure 2E). We generated the initial configuration of our modeled ion gel structure through random packing of [EMIM][TFSI] and e-P(VDF:HFP) polymer matrix (close to 55 wt% IL). The initial configuration was then subjected to long equilibration at 1000 K, followed by a fast thermal quench to 600 K and then 300K (details

are described later on). The obtained configuration after thermal equilibration was used for studying the ion gel surface properties. We validated the modeled ion gel structure by characterizing the gel ionic conductivity and comparing with the ionic conductivity of IL, as measured from the MD simulation trajectories. Details of the ion gel structure modeling procedures are described below.

Starting structure of e-P(VDF:HFP) polymer matrix. The e-P(VDF:HFP) polymer matrix was modeled as a triblock copolymer chain with 30 VDF units and 30 HFP units ($(VDF)_{15}(HFP)_{30}(VDF)_{15}$). Although the average molecular weight of the actual copolymer chains is much larger than that of our model, we aimed to utilize a simplified representation of the copolymer chain to model the local ion gel structure. To build an e-P(VDF:HFP) chain, individual blocks were first constructed and equilibrated in IL environment. Next, the equilibrated blocks were connected to build the full-length copolymer chain followed by further equilibration. Detailed steps of building the copolymer chain are as follows:

1) Single polymer chains, each containing 15 VDF or 15 HFP monomers, were constructed using Maestro[8] and optimized by its built-in Geometry Cleanup function.

2) The optimized VDF and HFP polymer chains were mixed with 480 IL ionic pairs (structures drawn with Maestro[8]) in orthogonal simulation boxes. A series of MD simulations were performed to equilibrate the systems in the following order:

I. 10,000 steps of minimization.

II. 1 ns heating from 0 to 10 K in NVT ensemble.

III. 1 ns equilibration at 10 K in NPT ensemble.

IV. Heating from 10 to 600 K and maintaining the system at 600 K in NPT ensemble for 10 ns.

V. Annealing to 300 K and maintaining the system at 300 K in NPT ensemble for 10 ns.

3) After equilibration, the final conformations of VDF and HFP chains were connected to build the triblock copolymer chain $(VDF)_{15}(HFP)_{30}(VDF)_{15}$ using Chimera[9].

4) e-P(VDF:HFP) chain was mixed with 960 [EMIM][TFSI] ionic pairs. The system was then subjected to equilibration using the protocols similar to step 2. The resulting conformation was used as the initial structure of triblock copolymer chain for the next steps.

Starting structure of the bulk ion gel. The obtained starting structure of e-P(VDF:HFP) chain, $[EMIM]^+$ and $[TFSI]^-$ were utilized to build the bulk ion gel configuration. The initial bulk configuration of the ion gel was randomly generated using the Packmol[2] and followed by equilibration at high temperature and subsequent thermal quench. Based on our XPS results, the template with 80 wt% IL in the pre-gel solution contains 55 wt% IL in the top surface. Therefore, the simulated ion gel was made of 34 e-P(VDF:HFP) chains and 560 [EMIM][TFSI] ionic pairs. The initial dimensions of the simulation orthogonal box were 100×100×50 Å. After 10000 steps of energy minimization, the system was slowly heated for 1 ns from 0 to 10 K in NVT ensemble and maintained at 10 K for another 1 ns. Next, the system was slowly heated from 10 to 1000 K and maintained at 1000 K for 5 ns. After equilibration at high temperature, the system was cooled down to 600 K and equilibrated for 5 ns. Finally, all the systems were cooled down to 300 K and equilibrated for 5 ns. The resulting bulk configuration was used for further simulation studies.

Validating the ion gel bulk structure using ionic conductivity measurements. To validate the accuracy of the obtained ion gel bulk structure after equilibration, we calculated the ionic conductivity for both the ion gel and the neat IL from simulations and compared it with the experimental results obtained from electrochemical impedance spectroscopy. We performed 20 ns

of MD simulations on the bulk of the neat IL and the ion gel (Figures S7 and S8, simulation IDs #1 and #2 in Table S1). For the neat IL simulation, 280 ionic pairs were packed into a cubic simulation box. For the ion gel simulation, the equilibrated structure after thermal quench was employed. The simulations were performed at constant temperature and constant pressure (300 K and 1 atm (NPT)) with periodic boundary conditions. The trajectories were saved every 2 ps and 10,000 frames were used for the calculation of IL diffusion constants using the Einstein equation (equation 1):

$$D_i = \frac{1}{6}\lim_{t\to\infty} \frac{d}{dt} < [r_i(t) - r_i(0)]^2 > \quad (1)$$

The calculation of diffusion constant was performed using the CPPTRAJ in AMBERTools14[9]. Ionic conductivity was then estimated from the Nernst-Einstein equation[10] using diffusion constants of cation and anion (equation 2):

$$\sigma = \frac{ce^2(D_{cation} + D_{anion})}{k_B T} \quad (2)$$

where c is the charge carrier number concentration ($c = {N_c}/{V}$), e is the charge of cation and anion, k_B is the Boltzmann constant, and T is the temperature.

MD simulations on the ion gel under the vacuum. To characterize the ion gel interfacial characteristics under the vacuum, we performed MD simulation of the equilibrated ion gel configuration (simulation ID #3 in Table S1). Herein, a large vacuum layer was added along the z dimension of periodic simulation box. As a result, the z dimension of the simulation box increased from 46 to 200 Å while the x and y dimensions remained unchanged. The simulation was performed at 300 K in NVT ensemble with periodic boundary conditions. To mimic the physically cross-linked network of the e-P(VDF:HFP) chains, position restraints were applied on 5 backbone heavy atoms (evenly distributed along the copolymer backbone) with a force constant of 2 kcal

mol^{-1}. We ensured that the overall e-P(VDF:HFP) chains remained dynamic. A single simulation was launched on the equilibrated ion gel structure for a total simulation time of 240 ns. The details of simulating the ion gel interfacial properties upon exposure to chloroform is described in the next section.

2. MD simulations on DPP-BTz/chloroform and the ion gel template

To better understand the synergistic templating effect between [EMIM][TFSI] and e-P(VDF:HFP) which led to superior polymer chain alignment and crystallinity in ion gel-templated films, we performed MD simulations with full atomic details to realistically capture the molecular interactions between templates and conjugated polymer (Figure S8, simulation ID #4, Table S1). The simulation box contained two layers: the ion gel template and the DPP-BTz/chloroform solution (Figure 7A). Given the constraints on the simulation box size, the simulated DPP-BTz oligomer included 4 monomers and alkyl chains were shortened to almost 1/3 of the original lengths (Figure S20A). We acknowledge that approximating polymers with shortened lengths of backbone and alkyl chain is a limitation of our simulation study given the large system size. From the simulations on DPP-BTz/chloroform and the ion gel template we investigated the ion gel interfacial properties upon exposure to chloroform (mimicking the contact angle experiments).

The equilibrated configuration of the ion gel was employed as the templating substrate structure. The packed chloroform solution layers (containing single DPP-BTz oligomer and varying numbers of chloroform molecules) were added along the *z* dimension of the ion gel template. In total, 10 random initial configurations with DPP-BTz evenly distributed in the chloroform solution layer along the *z* direction of the periodic simulation box were generated. After 10,000 steps of energy minimization, each system was slowly heated from 0 to 10 K in NVT ensemble for 1 ns and subsequently maintained at 10 K (NPT ensemble) for 1 ns. Next, the system was slowly heated

from 10 to 300 K and maintained at constant temperature and pressure for 2 ns. Production runs were launched from the equilibrated configurations and performed in NPT ensemble (300 K, 1 atm). 10 parallel simulations were run each with a total simulation time of 240 ns.

ID	System	# Molecules	Simulation box (Å)	Simulation time (ns)
1	IL (bulk)	280 IL pairs	49×49×49	20
2	Ion gel (bulk)	560 IL pairs, 34 copolymer chains	97×97×46	20
3	Ion gel (vacuum)	560 IL pairs, 34 copolymer chains	97×97×200	240
4	Ion gel with DPP-BTz	560 IL pairs, 34 copolymer chains, 1 DPP-BTz, 13800 $CHCl_3$	101×102×227	240×10

Table S1. Summary of molecular dynamics simulations details. The simulation box dimensions after equilibration were given.

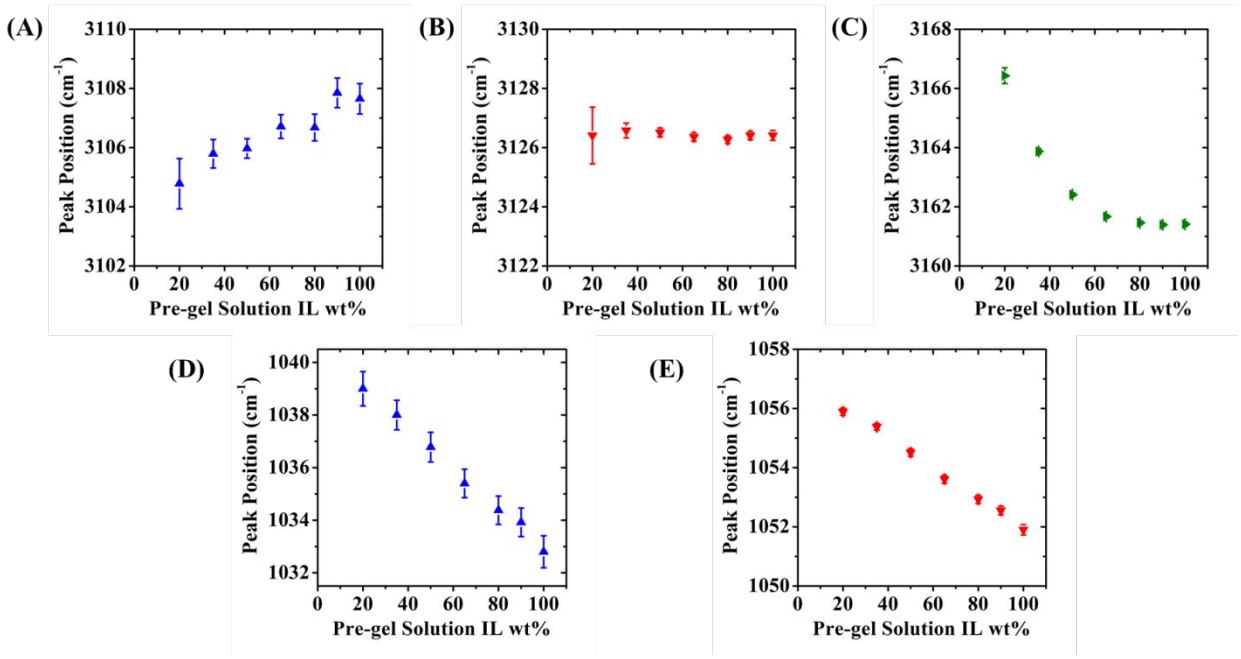

Figure S1. [EMIM][TFSI] ATR-FTIR characteristic peak positions in ion gel templates as a function of IL wt% in the pre-gel solution. (A-C) Peak shifts corresponding to C-H vibration in the cation imidazole ring within wavenumbers of 3100-3170 cm^{-1}. (D, E) Peak shifts corresponding to SNS antisymmetric stretching from 1025-1075 cm^{-1}.

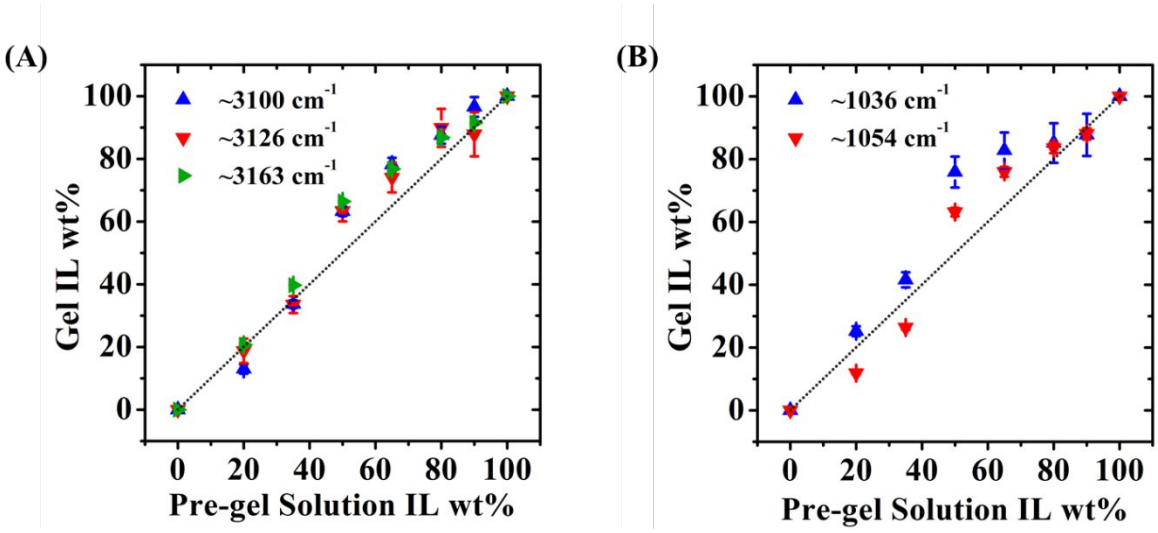

Figure S2. Estimated IL wt% in the bulk of the ion gel using ATR-FTIR vibrational peaks. A) IL wt% extracted from three different peaks assigned to C-H vibration of cation's imidazole ring within wavenumbers of 3100-3170 cm-1. B) IL wt% estimated from two peaks which are attributed to anion SNS antisymmetric stretching from 1025-1075 cm^{-1}.

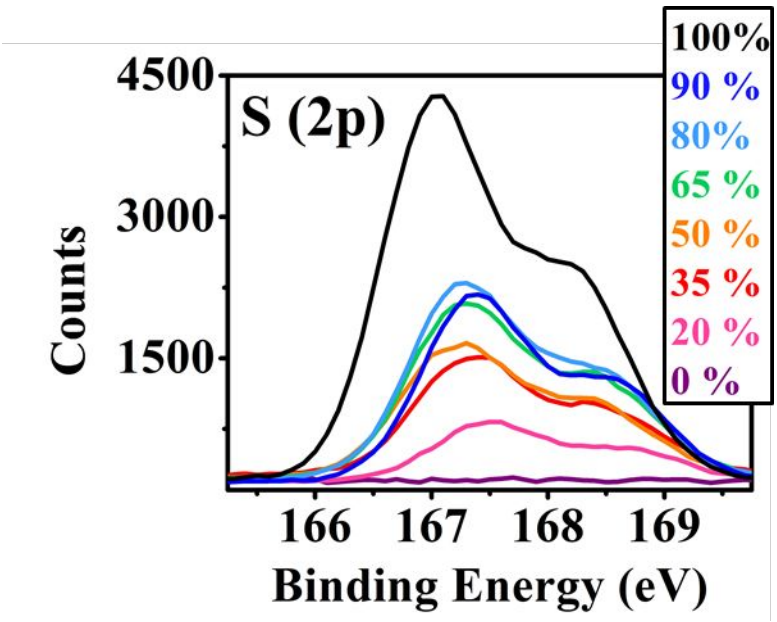

Figure S3. High resolution XPS spectra of the S (2p) region obtained for various ion gel composition in terms of pre-gel IL wt%.

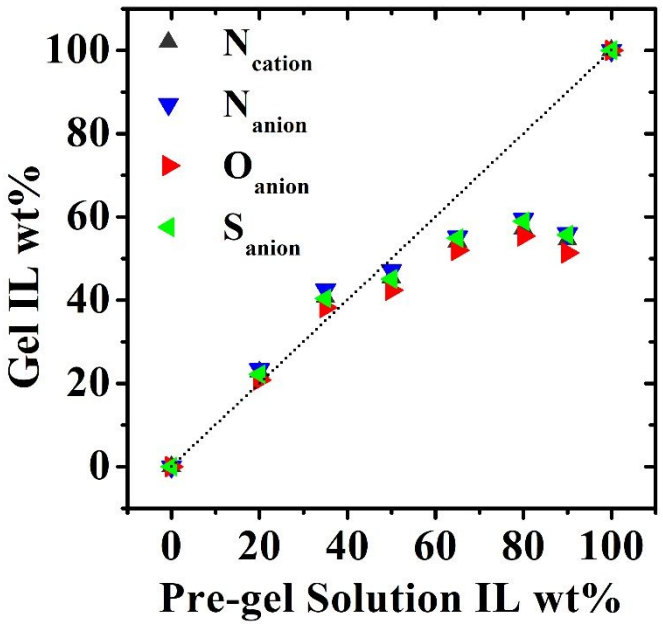

Figure S4. Estimated IL wt% at the ion gel surface extracted from high resolution spectra of N (1s), O (1s) and S (2p). N (1s) spectral features can be resolved by fitting two distinct peaks centered at ~397.5 eV and 400.1 eV which originated from [$TFSI^-$] anion and cation's imidazole ring, respectively. Moreover, we deconvoluted high resolution spectra of [$TFSI^-$] anion's O (1s) (peak centered at 530.6 eV) and S 2p (doublet at 167.1 and 168.2 eV). We analyzed all these peaks using CasaXPS software and compared the peak area for each element to that of the neat [EMIM][TFSI] to calculate IL wt% and plotted the averaged values. Our results convey that the ion gel surface, when in high vacuum, is enriched with the e-P(VDF:HFP) polymer matrix possibly due to its lower surface tension relative to [EMIM][TFSI] at high IL content.

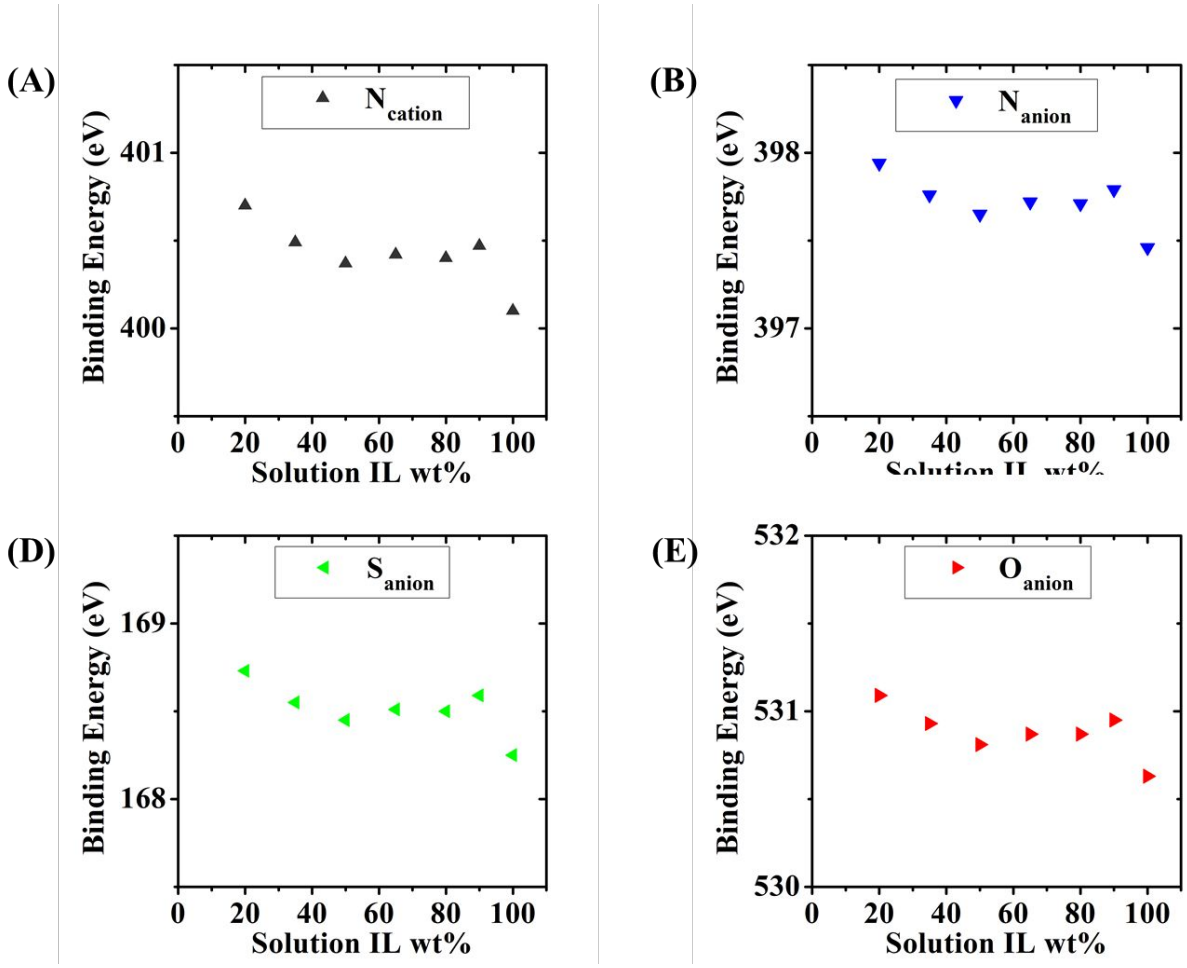

Figure S5. Peak shifts in high resolution XPS spectra of ion gel as a function of pre-gel IL wt%. A) Cation's N (1s), B) Anion's N (1s), C) O (1s), and D) S (2p).

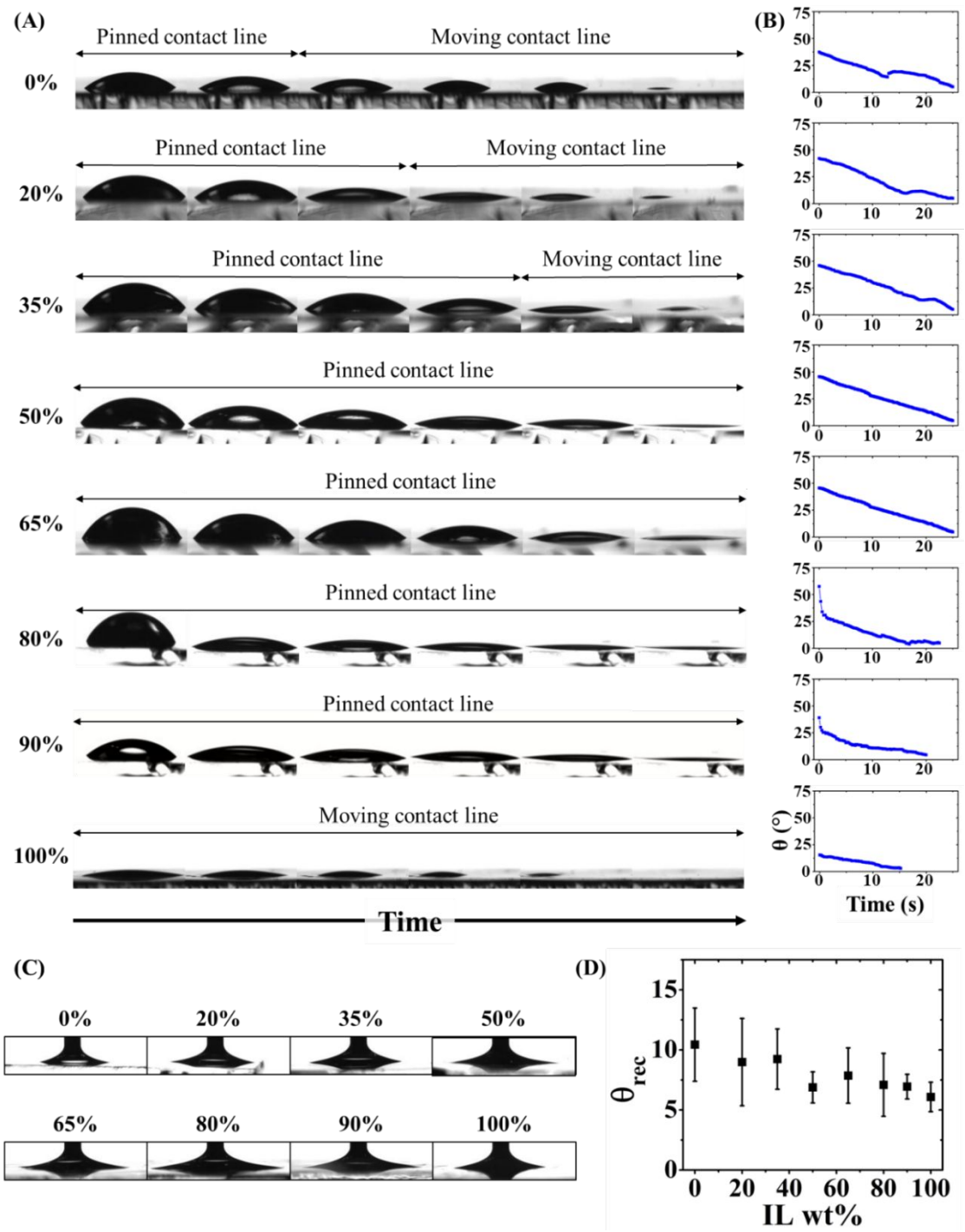

Figure S6. Chloroform contact angle measurements on various templates. (A) Optical image of CF sessile drop evaporation and (B) time-dependent CF contact angle on ion gel templates with varying IL content. (C) Optical image of CF receding meniscus on various templates and (D) receding contact angle of CF as a function of IL content in the ion gel. A slight decreasing trend was observed for the CF receding contact angle. However, this trend was less sensitive to the template compared to the sessile drop experiment due to the capillary force imposed by the needle (similar to the coating blade in MGC).

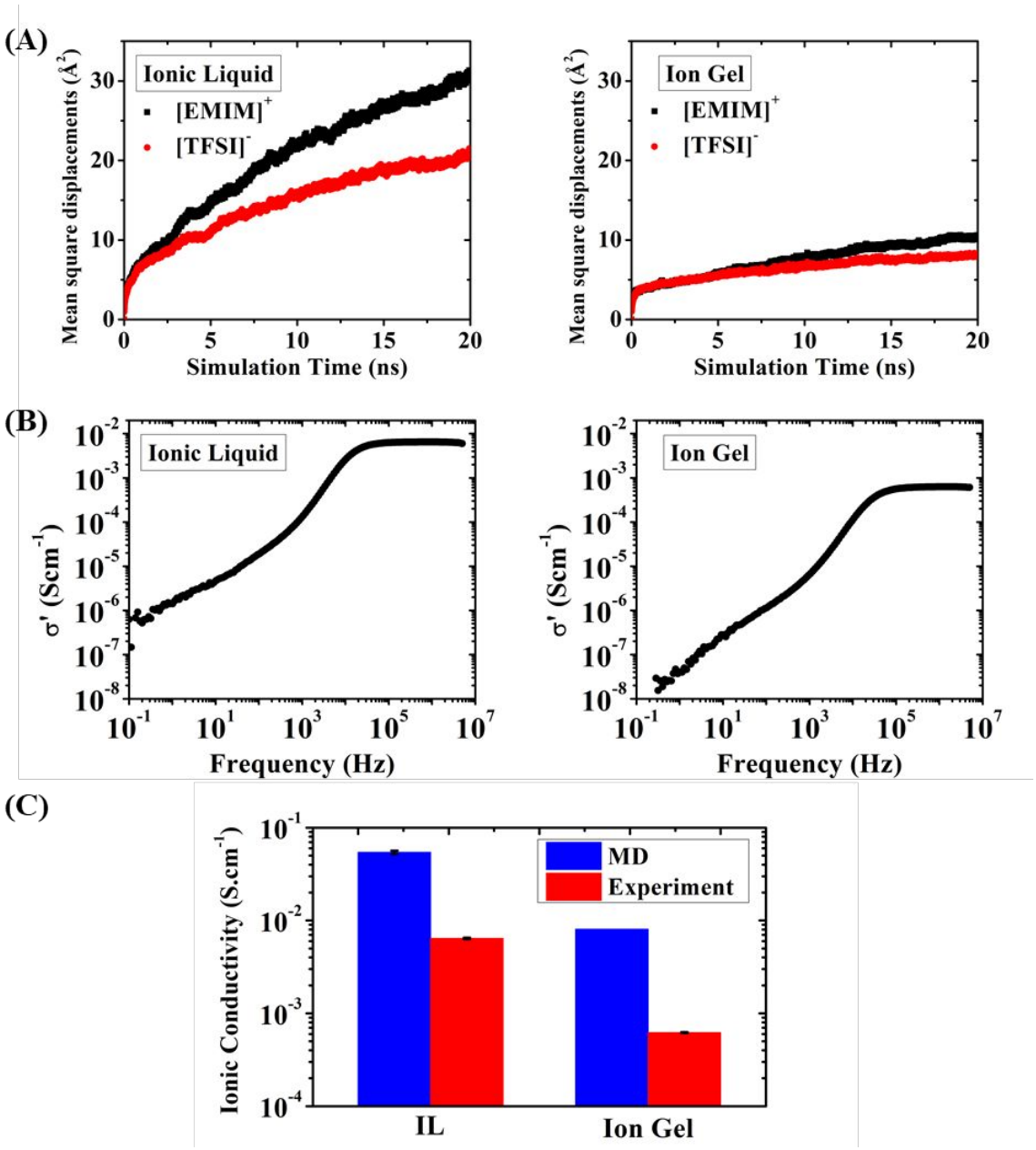

Figure S7. Validation of the ion gel bulk structure for MD simulations. (A) Overall mean square displacement of cations and anions with respect to the simulation time in the bulk of the neat IL and the ion gel (55 wt% IL) calculated from 20 ns MD simulations. (B) Frequency-dependent conductivity measurements from impedance spectroscopy comparing the neat IL and the ion gel. (C) Comparison between the bulk ionic conductivity obtained from MD simulation and electrochemical impedance spectroscopy. Adding polymer matrix to the IL led to a decrease in ionic conductivity evident from both MD simulations and experimental data.

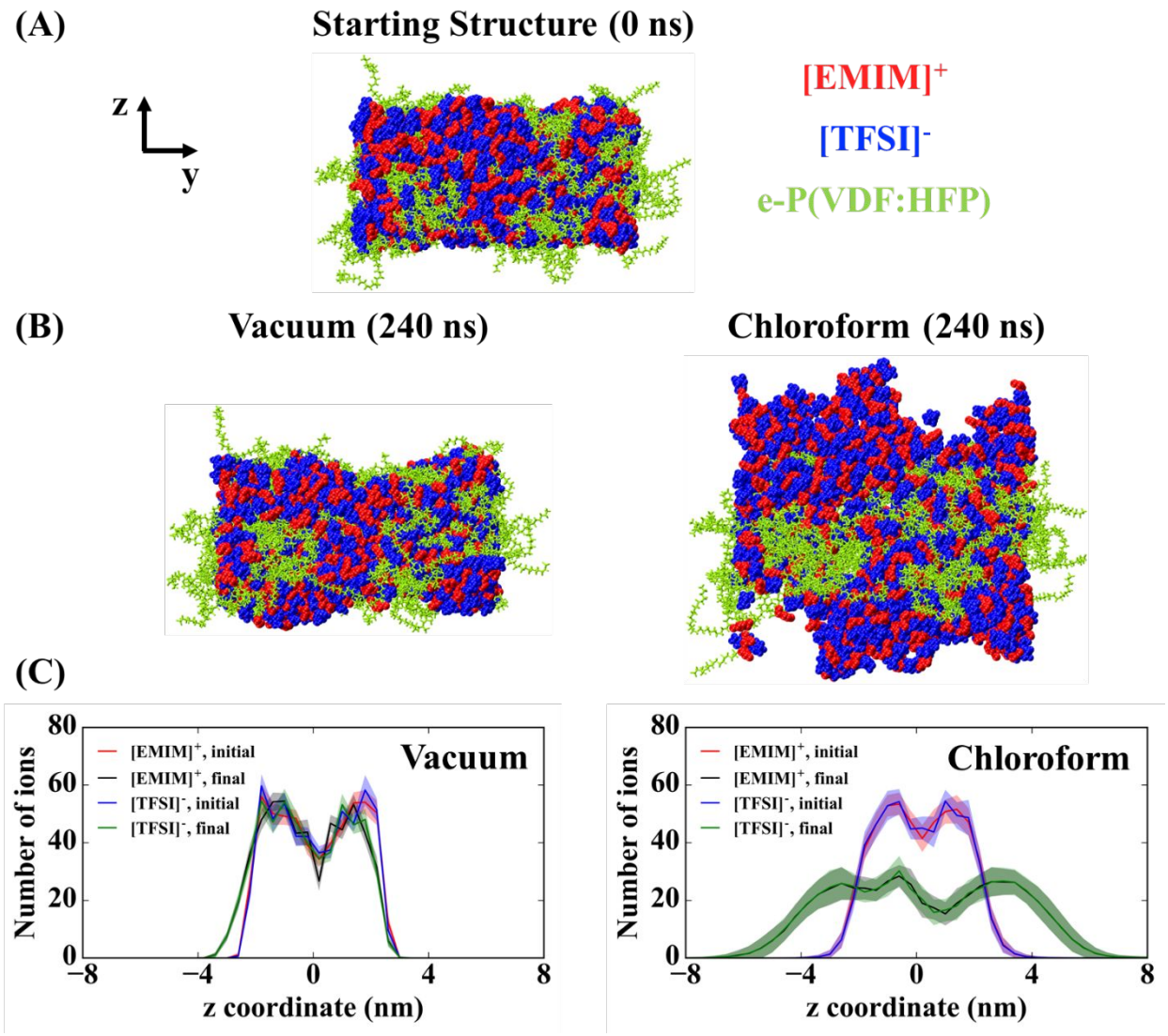

Figure S8. Ion gel interfacial properties predicted by MD simulations. (A) The ion gel (~55 wt% IL) starting structure set up for MD simulation studies. $[EMIM]^+$ and $[TFSI]^-$ are shown in red and blue. (B) Snapshots of the ion gel surface after exposure to vacuum environment and solvent molecules (chloroform) after 240 ns of simulation. The solvent molecules are omitted for clarity (C) IL cation and anion distribution along the z axis (orthogonal to the ion gel surface) upon exposure of the ion gel surface to vacuum and chloroform at the initial (first 10 ns) and final (last 10 ns) steps of MD simulations. The bin size of z coordinate is 0.4 nm. The number of $[EMIM]^+$ and $[TFSI]^-$ within each bin region are counted based on the z coordinates of their center of mass.

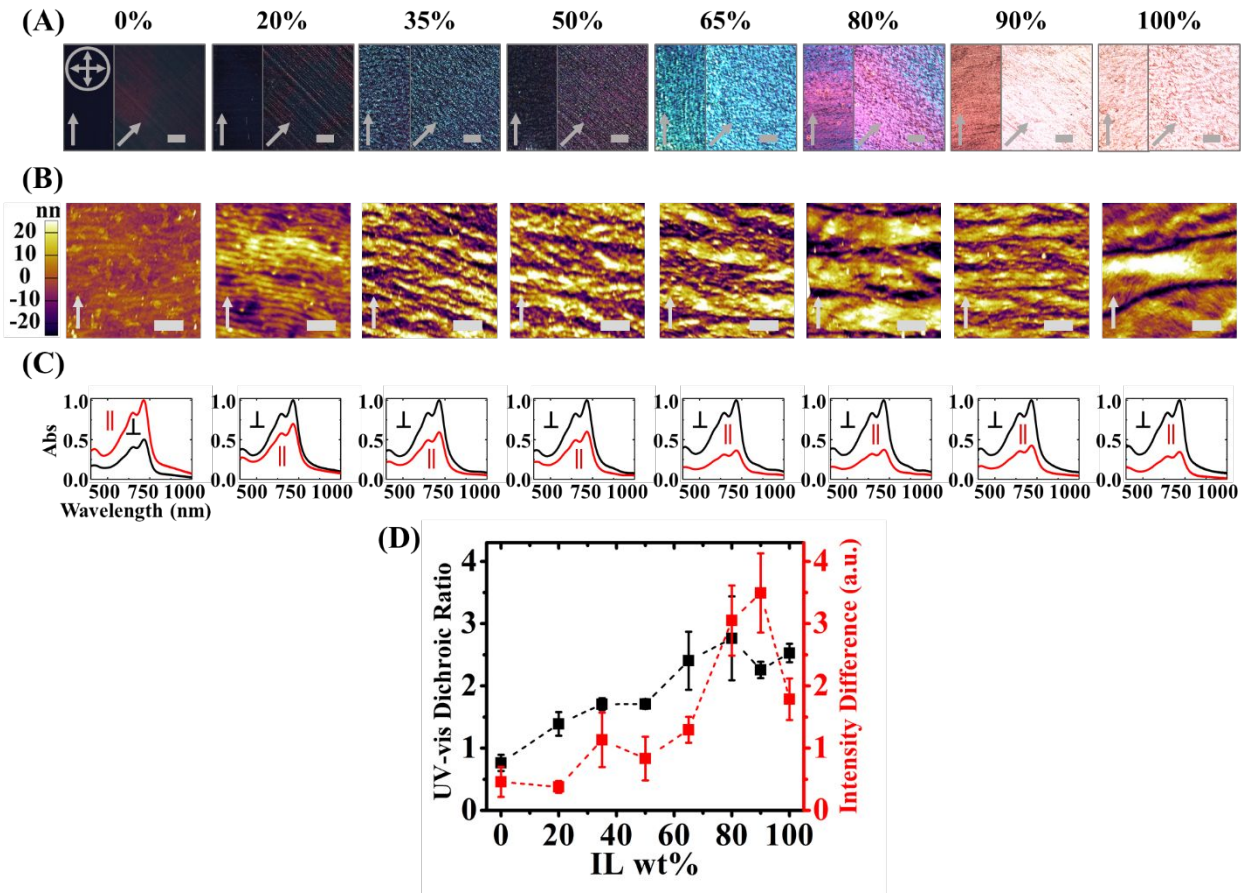

Figure S9. Macro- and meso-scale morphology of PII-2T films coated on various dynamic templates. (A) Cross-polarized optical microscopy images. The orientation of crossed polarizers is denoted as crossed arrows and the single arrow shows the coating direction. All scale bars are 100 μm. With increasing IL content in the template, stronger birefringence effect is observed in templated PII-2T thin films. Upon rotation, the whole C-POM image uniformly varies in intensity which indicates that the film is highly aligned at the macroscale. (B) Tapping-mode AFM height images with 2 μm scale bars, showing increase in domain size with the increase of IL content in the template. (C) Normalized absorption spectra of polarized UV-vis spectroscopy, where the sign ∥ (⊥) denotes the film orientation when the coating direction is parallel (perpendicular) to the axis of the polarizer. (D) Polarized UV-vis dichroic ratio (black) and C-POM birefringence (red) as a function of the IL content in the template with a maximum at 80 and 90 wt% IL. The birefringence is calculated as the difference between the average intensities when the film is oriented 45^0 vs. 0^0 with respect to the polarizer axis (Fig. S7A). Error bars were obtained from multiple measurements on one sample.

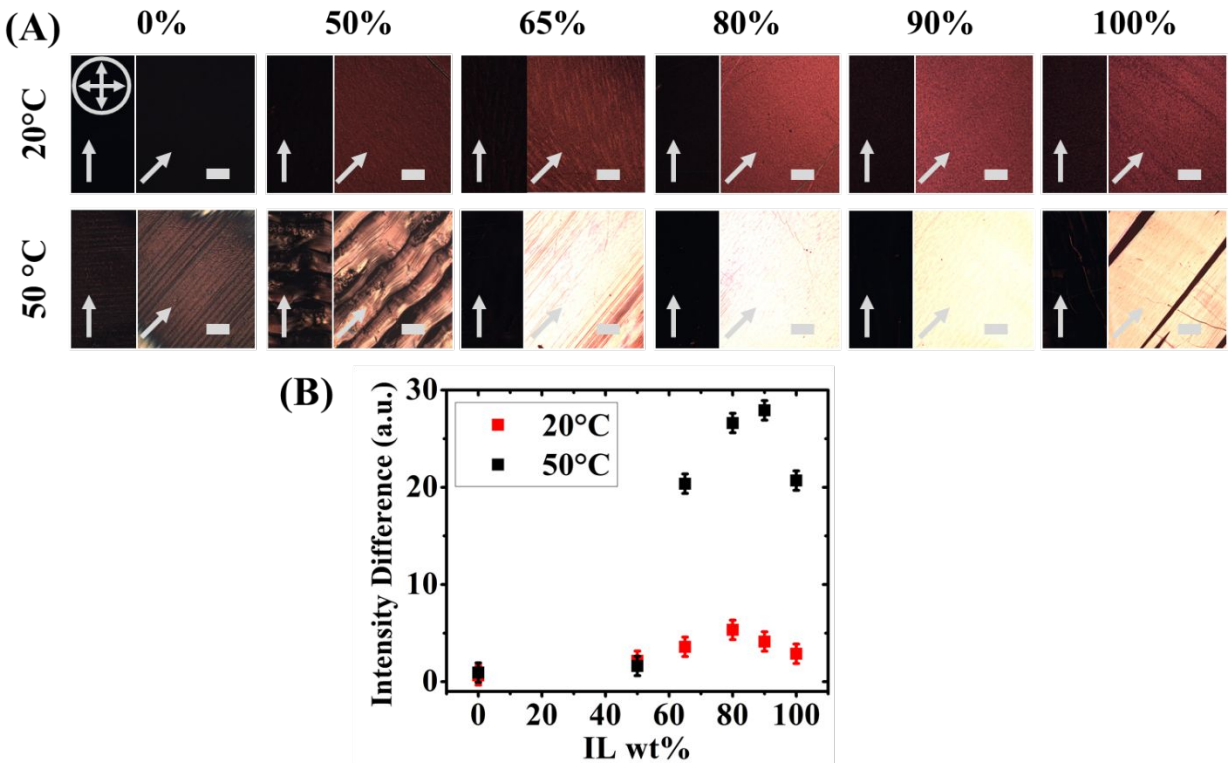

Figure S10. The influence of the deposition temperature on DPP-BTz thin film morphology. (A) C-POM images of DPP-BTz films coated at 20°C and 50°C on various. The orientation of crossed polarizers is denoted as crossed arrows and the single arrow shows the coating direction. All scale bars are 100 μm. With increasing IL content in the template (at constant temperature), DPP-BTz thin films become more aligned and/or crystalline. Furthermore, upon increasing the deposition temperature the optical birefringence significantly increases. (B) C-POM intensity difference as a function of the template IL content. The birefringence is calculated as the difference between the average intensities when the film is oriented 45^0 vs. 0^0 with respect to the polarizer axis normalized with 0^0 image intensity.

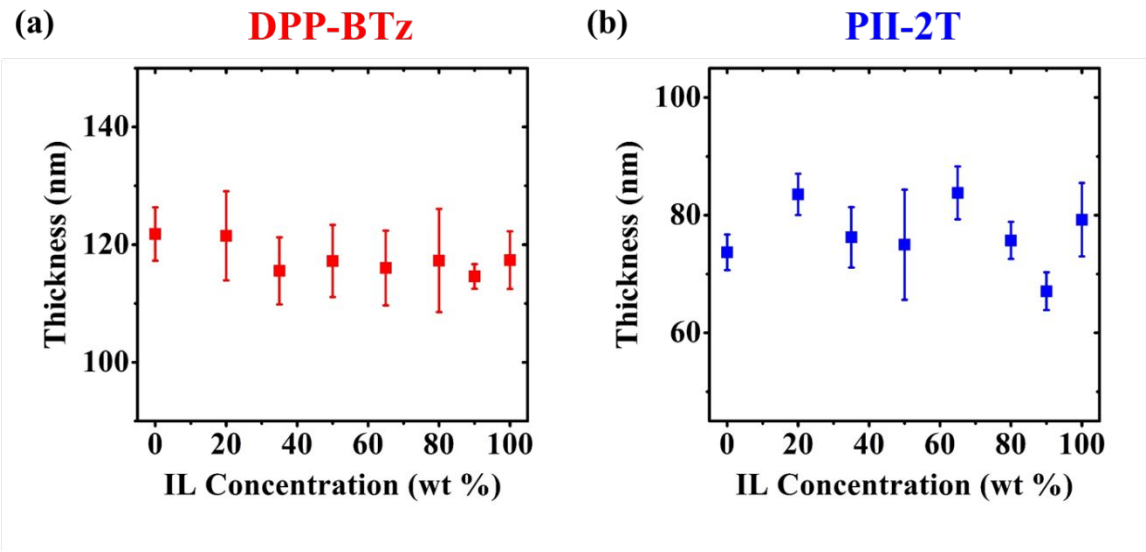

Figure S11. Relationship between polymer film thickness and template composition. (a) DPP-BTz, (b) PII-2T film thicknesses were determined from the cross-sectional profile of the tapping-mode AFM images. This result shows that film thickness is independent of the IL concentration in the template, when coated at the same conditions (see Methods).

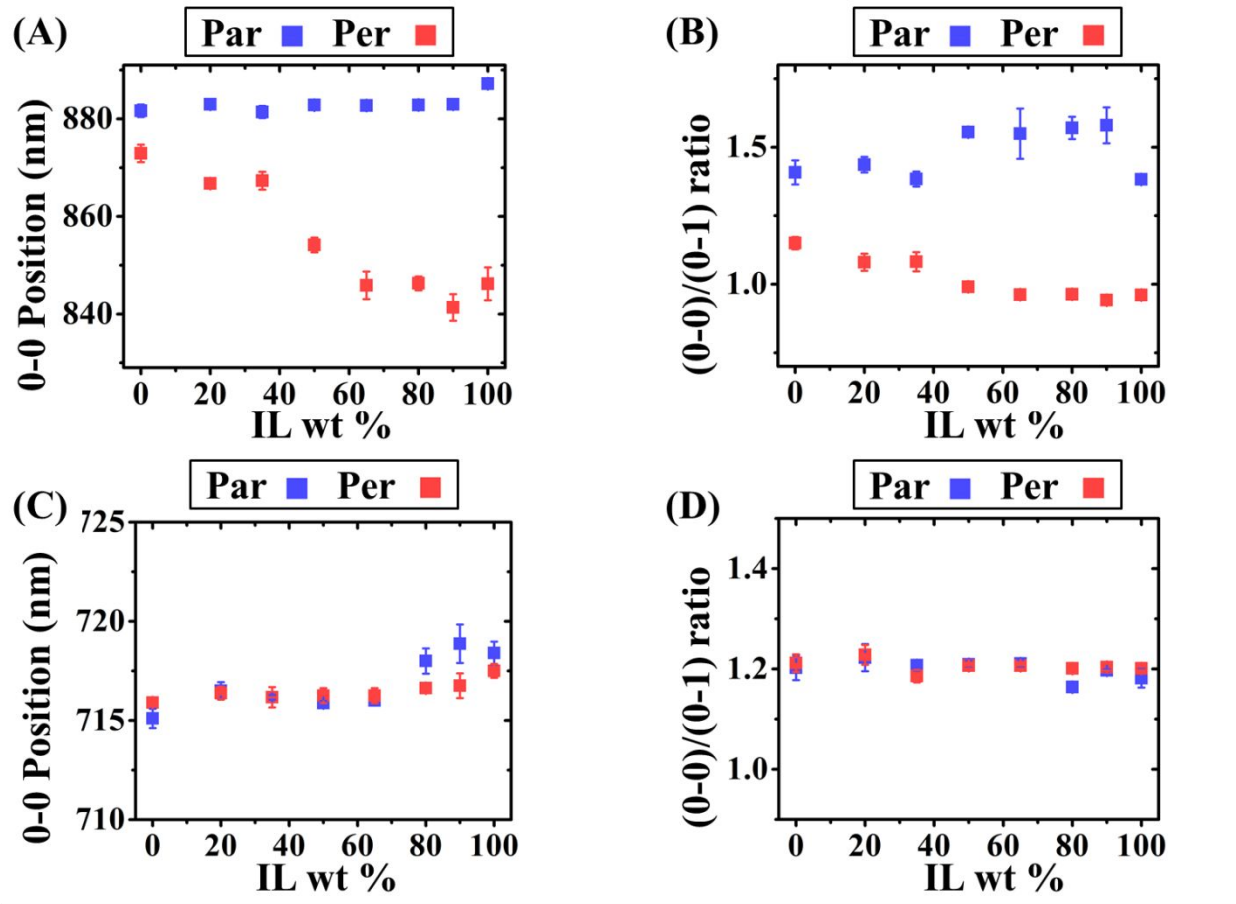

Figure S12. Peak analysis of template-composition-dependent polarized UV-vis spectra. 0-0 peak position and 0-0 to 0-1 vibronic peak ratio as a function of ion gel composition for (a-b) DPP-BTz and (c-d) PII-2T thin films measured with the coating direction parallel and perpendicular (red and blue data points) to the polarizer axis.

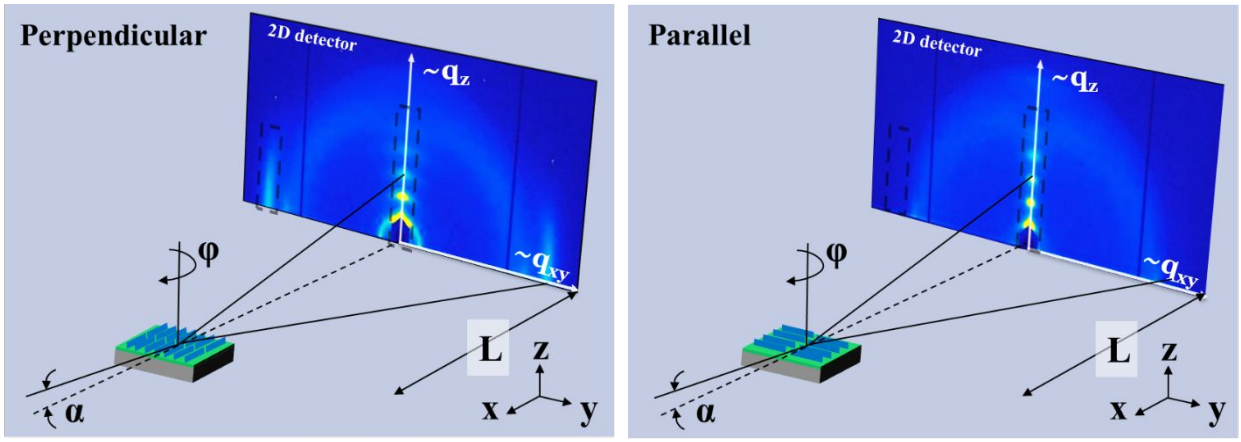

Figure S13. Grazing incidence X-ray diffraction (GIXD) measurements set-up. GIXD configuration measured via a two-dimensional image plate detector with an incident angle (α) of 0.2° and in-plane substrate rotation angle (φ) of 0° to 90° (parallel and perpendicular to the coating direction respectively). The polar angle, χ, denotes the out-of-plane orientation of the π-stacks (or lamellar stacks), with $\chi = 0°$ (90°) representing "face-on" ("edge-on") orientation with respect to the substrate's normal. Dichroic ratio (R) based on π- π stacking was calculated as $R = A_{\perp}/A_{\parallel}$, where $A_{\perp}$ and $A_{\parallel}$ represent the area of the edge-on π–π stacking peak normalized with film's irradiated volume with the incident beam perpendicular ($\varphi = 90°$) and parallel ($\varphi = 0°$) to the coating direction, respectively.

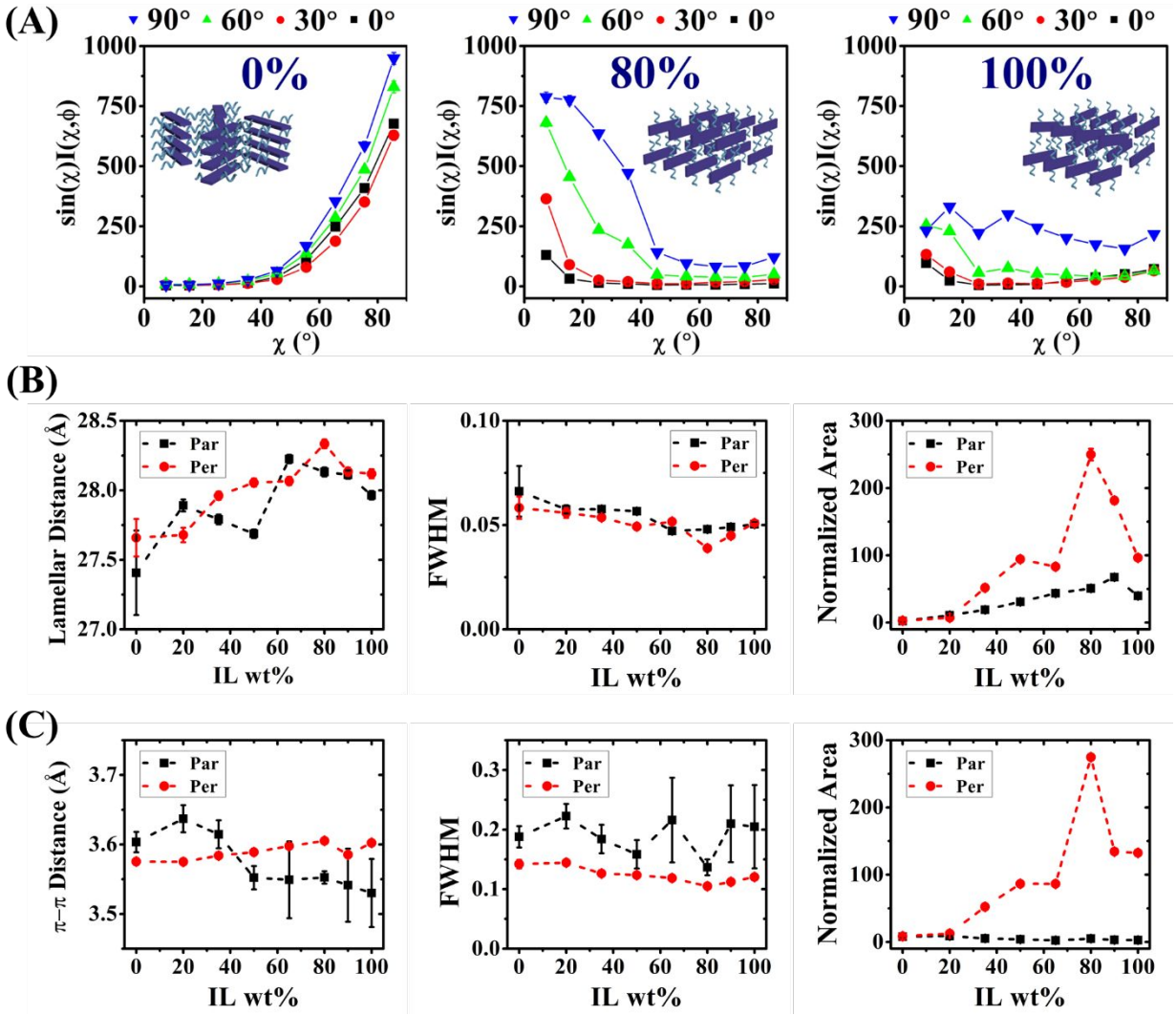

Figure S14. DPP-BTz thin film GIXD orientation and peak analysis. (A) Path length corrected intensity of DPP-BTz lamellar stacking, extracted from (200) peak, as a function of χ and φ on templates with 0%, 80% and 100% IL which were transferred to OTS-treated silicon wafers prior to measurements. GIXD data were acquired through rotating the substrates in-plane by φ = 0° (parallel), 30°, 60°, and 90° (perpendicular) with respect to the incident beam. Error bars are due to the standard errors of (200) peak areas from multipeak fitting. Polymer packing schematics are shown in the inset highlighting the increase in "edge-on" to "face-on" crystallites population as more IL is added to the template, with the maximum at 80% IL. Lamellar stacking in pure IL is isotropic. GIXD peak analysis for (B) π-π (010), and (C) lamellar stacking diffractions representing in-plane and out-of-plane crystallites packing.

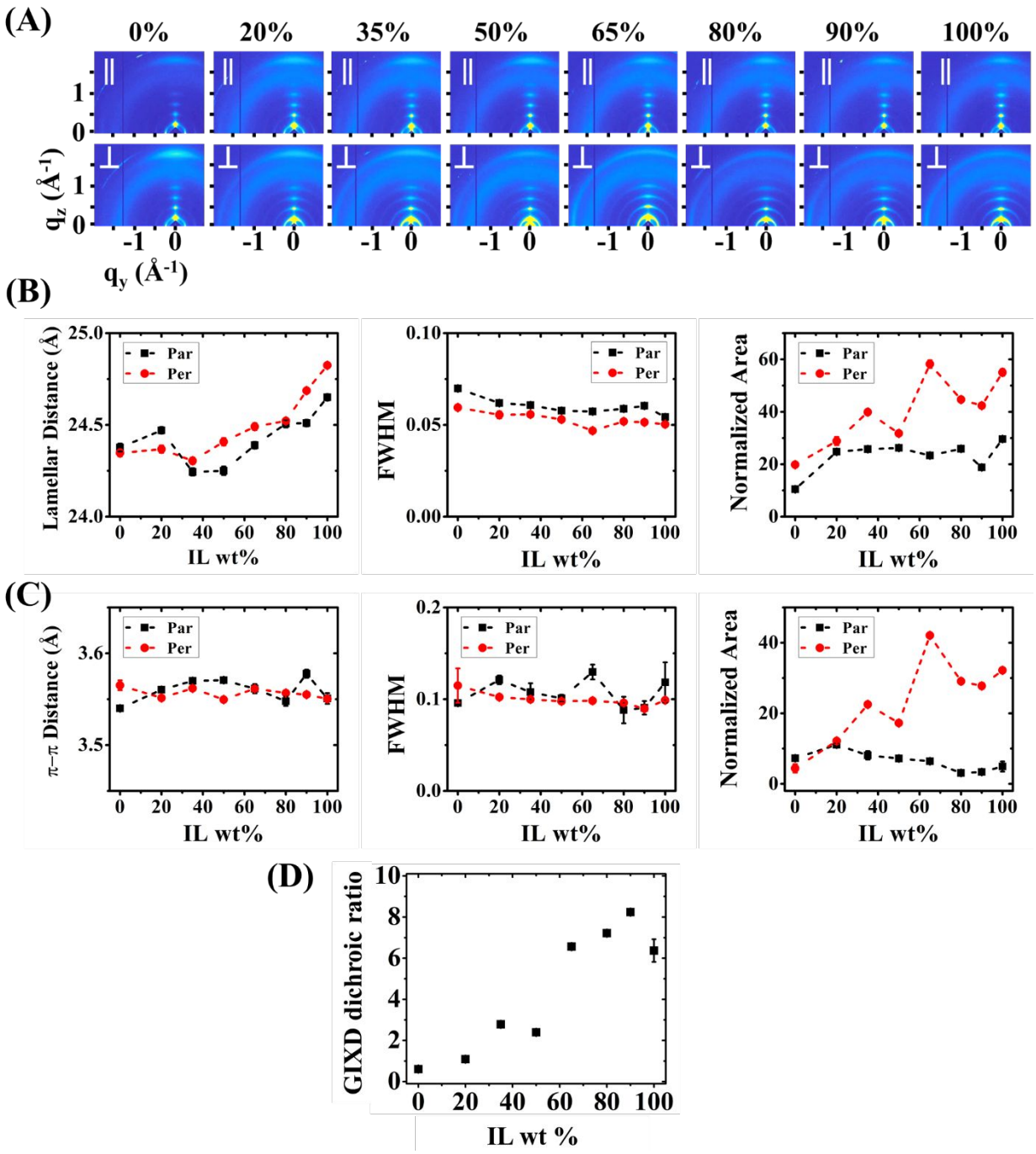

Figure S15. Quantifying PII-2T molecular packing, peak analysis, and anisotropy. (A) Comparison of GIXD patterns of films coated on templates with different elastomer to IL ratio, measured parallel and perpendicular to the coating direction with 0.2° incident angle (probing the bulk). Peak analysis for (B) π-π (010), and (C) lamellar stacking diffractions representing in-plane and out-of-plane crystallites packing. (D) Quantifying edge-on π–π stacking anisotropy by dichroic ratio (DR), with highest values at 90% and 80% IL respectively. Error bars are due to the standard errors of (010) peak areas from multipeak fitting.

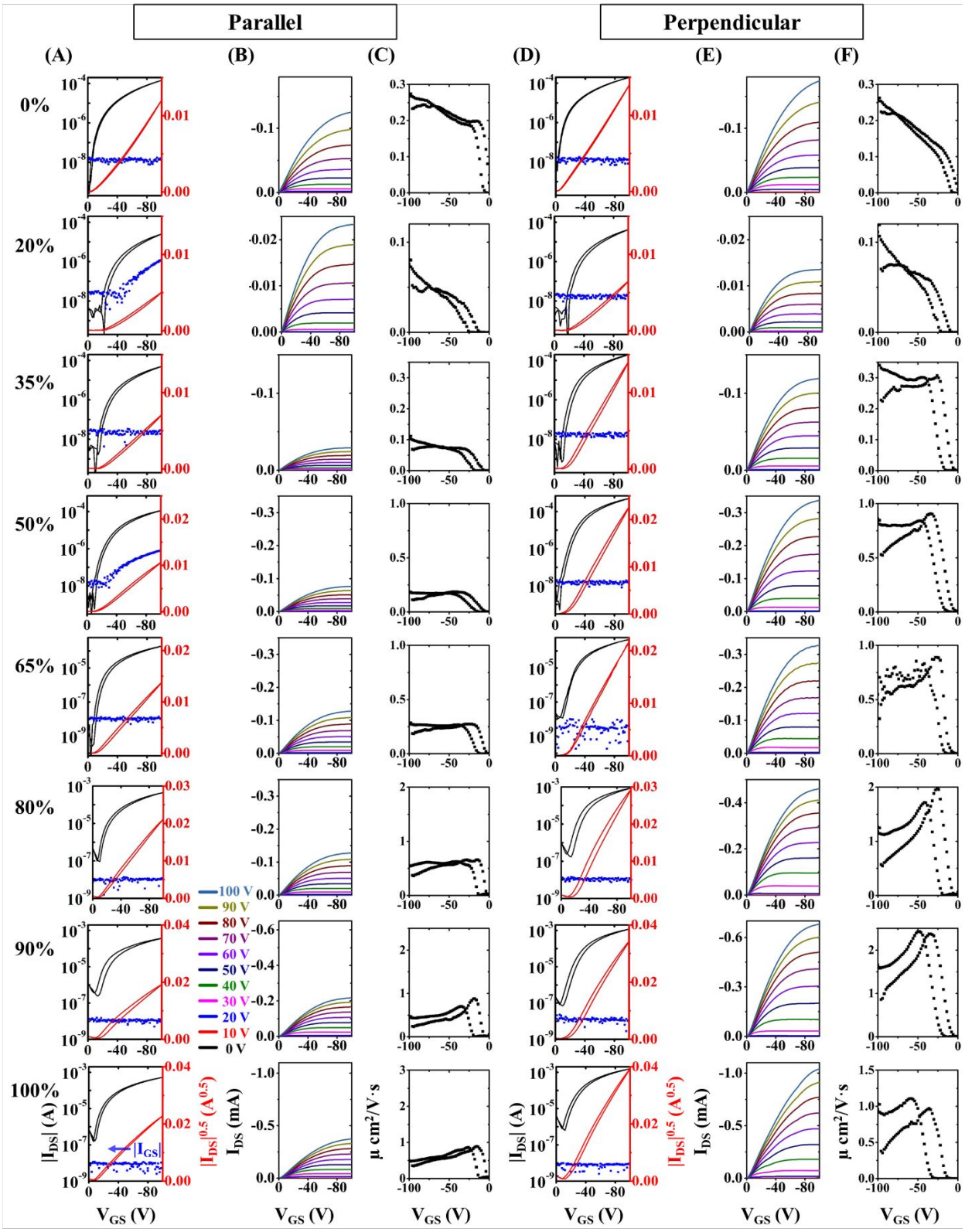

Figure S16. DPP-BTz thin film field-effect transistor characteristics. (A, D) transfer ($V_{DS} = -100V$), (B, E) output curves and (C, F) apparent hole mobility (extracted from saturation regime) as a function of

gate voltage, coated on various templates. The gate current (I_{GS}) in (A) and (D) is plotted (blue scatters) to assess the leakage current. DPP-BTz films were transferred to OTS-treated SiO_2 and BGTC structure was fabricated by thermally depositing MoO_3/Ag electrodes atop (W = 840 μm, L = 47 μm).

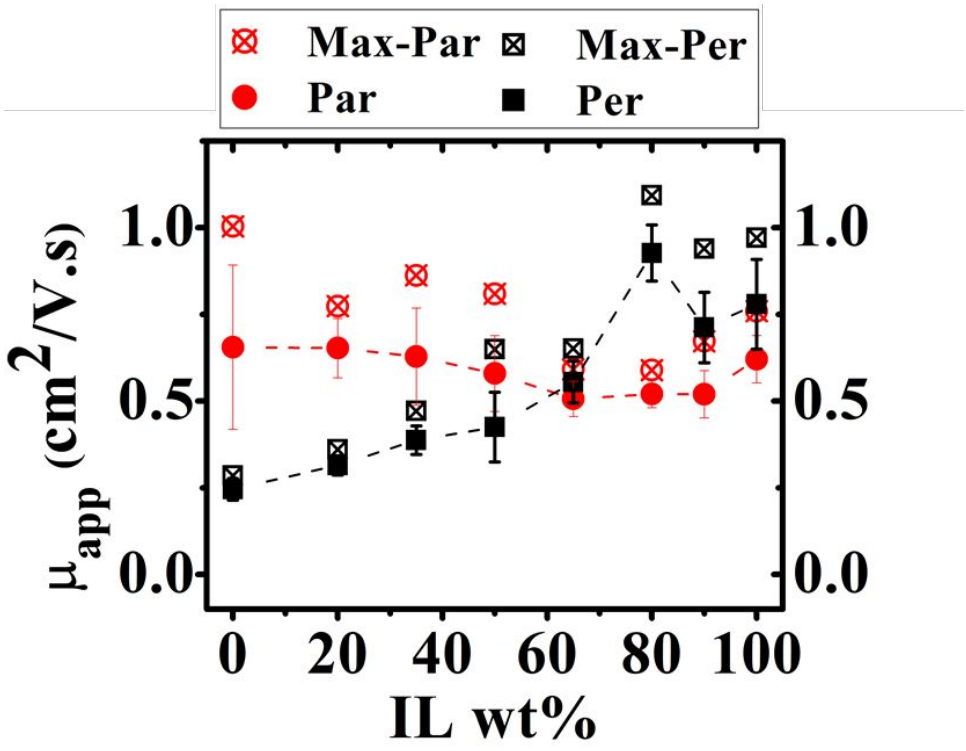

Figure S17. PII-2T charge transport properties in FET devices as a function of template IL content. Apparent hole mobility measured in parallel and perpendicular directions with respect to the coating direction as a function of template composition, extracted from saturation regime at V_{DS}= −100 V. Same device geometry and dimensions were adopted as in the DPP-BTz case.

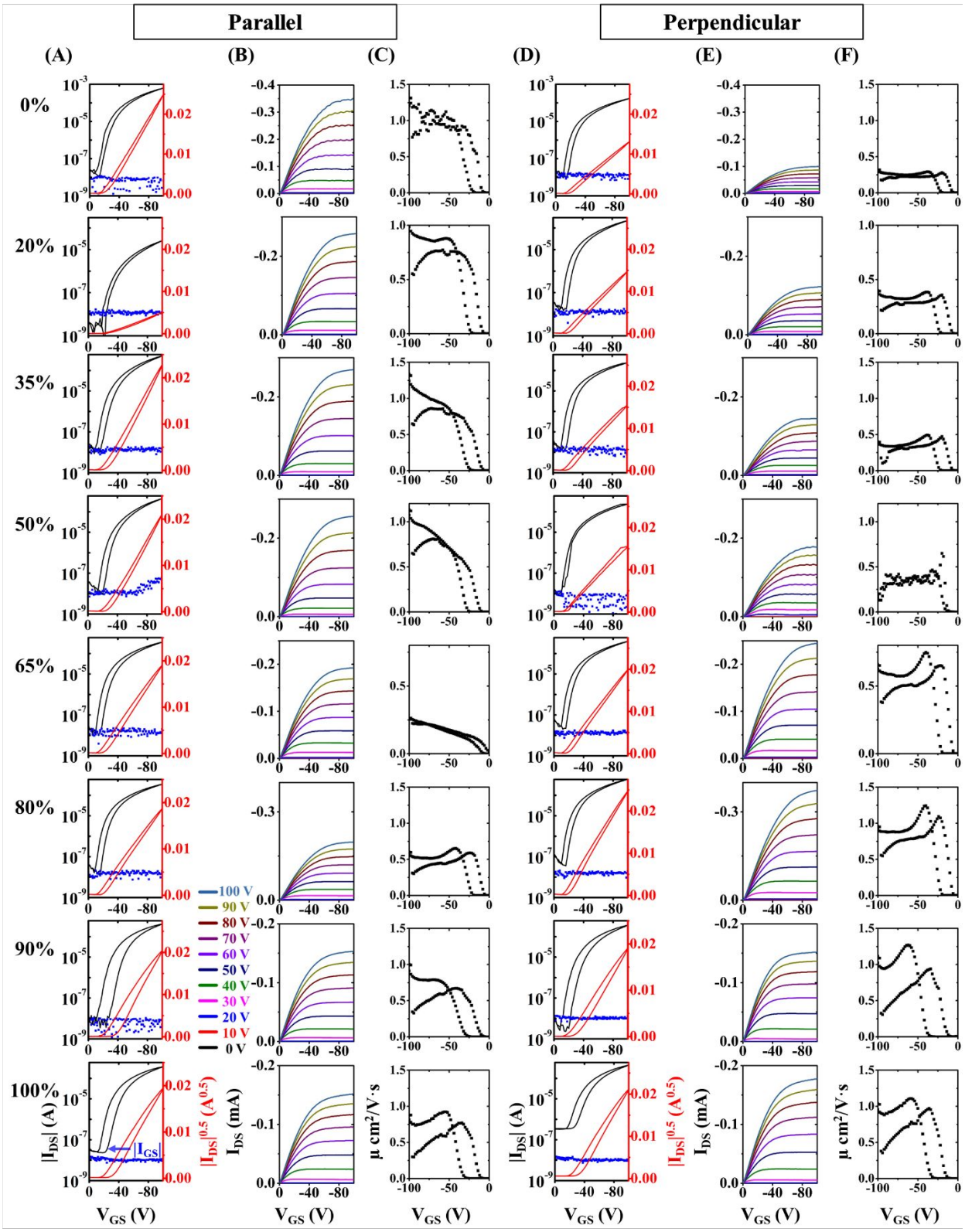

Figure S18. PII-2T thin film field-effect transistor characteristics. (A, D) transfer ($V_{DS} = -100$V), (B, E) output curves and (C, F) apparent hole mobility (extracted from saturation regime) as a function of gate

voltage, coated on various templates. The gate current (I_{GS}) in (A) and (D) is plotted (blue scatters) to assess the leakage current. PII-2T films were transferred to OTS-treated SiO_2 and BGTC structure was fabricated by thermally depositing MoO_3/Ag electrodes atop (W = 840 μm, L = 47 μm).

Substrate IL wt%	Parallel			Perpendicular		
	μ_{app} (max) ($cm^2V^{-1}s^{-1}$)	Log (I_{on}/I_{off})	V_{th} (V)	μ_{app} (max) ($cm^2V^{-1}s^{-1}$)	Log (I_{on}/I_{off})	V_{th} (V)
0	0.66±0.24 (1.00)	4.6±0.8	-14.5±1.5	0.25±0.03 (0.28)	4.3±0.6	-9.6±0.9
20	0.65±0.09 (0.77)	4.6±0.7	-18.5±3.3	0.31±0.03 (0.36)	4.2±0.4	-11.4±0.9
35	0.63±0.14 (0.86)	4.5±0.9	-16.4±1.3	0.39 ±0.04 (0.47)	4.3±0.6	-11.6±0.7
50	0.58±0.11 (0.81)	4.3±2.1	-14.6±4.4	0.42±0.10 (0.65)	4.2±1.6	-11.4±3.0
65	0.51±0.05 (0.59)	4.4±0.8	-14.0±0.6	0.55±0.06 (0.65)	4.3±0.9	-11.8±2.4
80	0.52±0.04 (0.59)	4.8±2.6	-14.5±3.1	0.93±0.08 (1.09)	4.8±2.2	-15.6±3.9
90	0.52±0.07 (0.67)	5.0±2.8	-15.9±2.6	0.71±0.10 (0.94)	5.1±2.5	-14.6±4.0
100	0.62±0.07 (0.76)	4.0±0.9	-12.1±2.7	0.78±0.13 (0.97)	4.2±1.2	-15.5±2.9

Table S2. Summary of the key FET parameters for PII-2T devices.

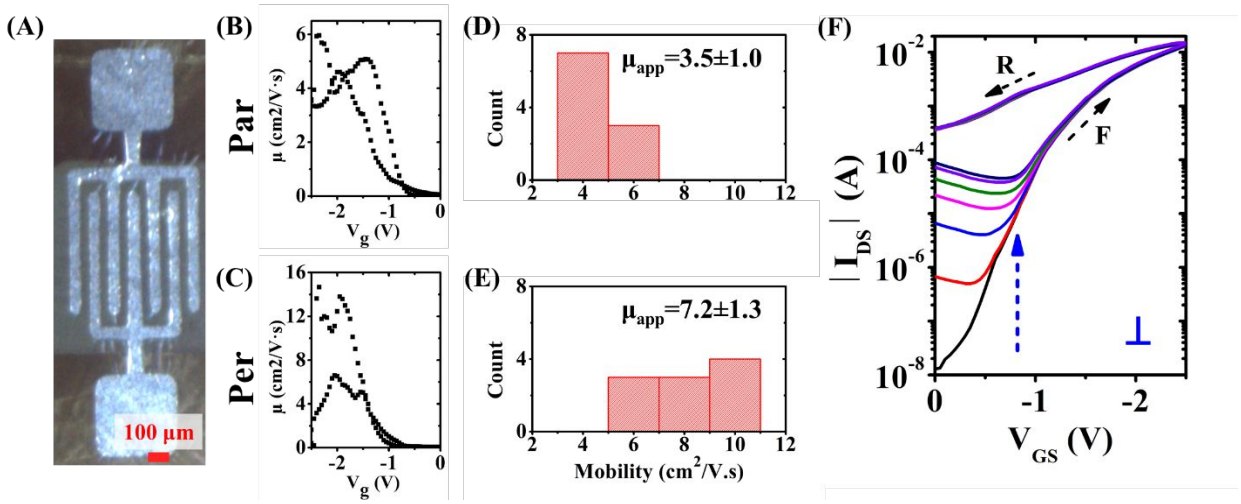

Figure S19. OECT devices with 80 wt% IL ion gel as the dynamic template and the dielectric layer. (A) Representative device optical microscopy image. (B and C) Gate-voltage-dependent apparent hole mobility plots corresponding to the transfer curves in Figures 6B and 6C. (D and E) Histograms of the hole mobilities calculated from 10 devices with the active channel parallel (F) and perpendicular (G) to the coating direction. Apparent hole mobility values averaged over the entire hysteresis loop from the saturation regime (V_{DS}= −1.5 V), were μ_{app}=3.5±1.0 $cm^2V^{-1}s^{-1}$ (parallel) and μ_{app}=7.2±1.3 $cm^2V^{-1}s^{-1}$ (perpendicular), respectively. (F) Measured I-V characteristics after 7 consecutive measurements showing increasing off-current due to dielectric ions migration towards semiconducting layer.

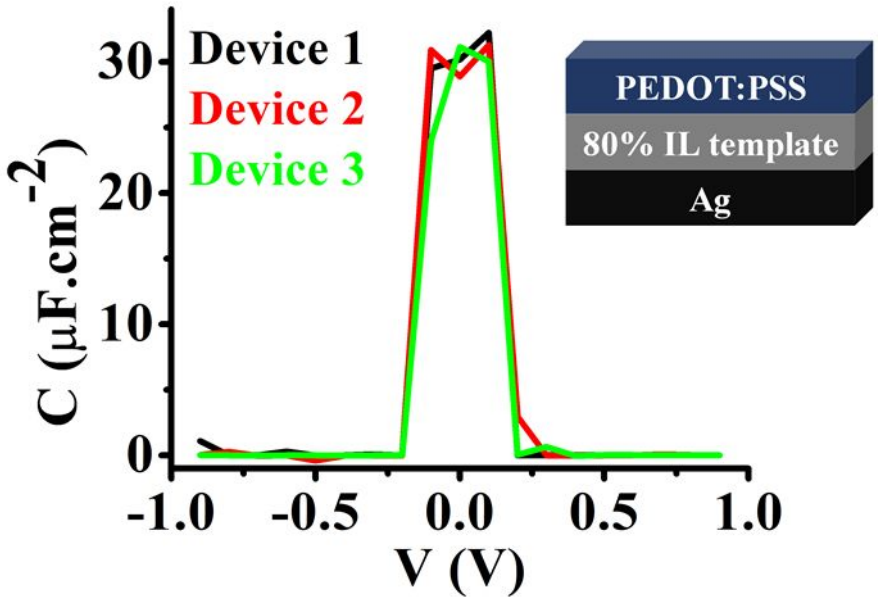

Figure S20. Voltage dependent quasi-static capacitance measurements of the 80% IL templates. Voltage dependence capacitance measurements with 0.1 V steps measured from -1 V to +1 V. In the inset the structure used for the measurements is depicted.

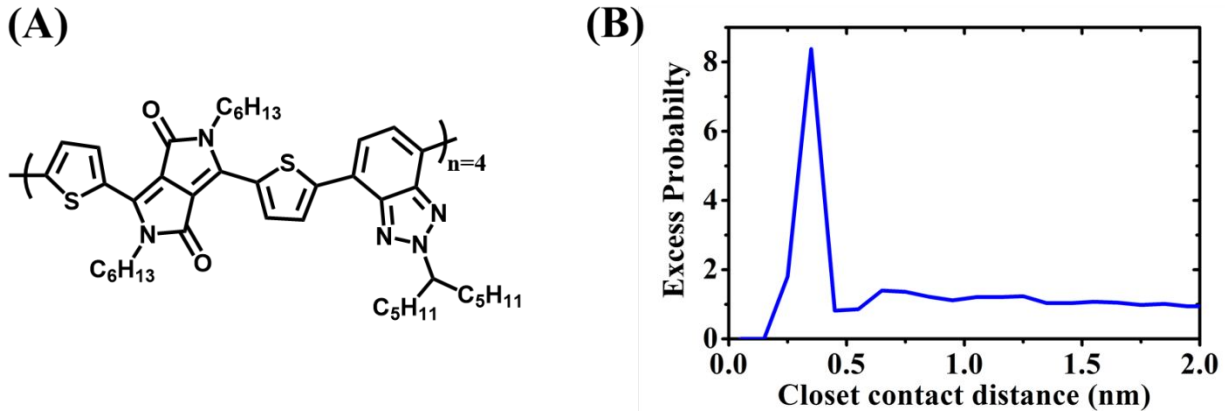

Figure S21. Simulated DPP-BTz structure and calculated excess probability distribution from MD. (A) Chemical structure of the employed DPP-BTz tetramer in MD simulations. DPP-BTz oligomer (tetramer) with reduced alkyl chains length is employed given the constraint on MD simulation box size to reduce the computation time to a reasonable time frame. (B) The excess probability distributions of the closest heavy atom distance between the DPP-BTz oligomer and the ion gel template. We normalized the distribution probability by the bulk value to directly compare the spatial distribution of the conjugated molecule near the ion gel surface with that of the bulk.

References

1. D.A. Case, I. Y. B.-S., S.R. Brozell, D.S. Cerutti, T.E. Cheatham, III, V.W.D. Cruzeiro, T.A. Darden, R.E. Duke, D. Ghoreishi, M.K. Gilson, H. Gohlke, A.W. Goetz, D. Greene, R Harris, N. Homeyer, S. Izadi, A. Kovalenko, T. Kurtzman, T.S. Lee, S. LeGrand, P. Li, C. Lin, J. Liu, T. Luchko, R. Luo, D.J. Mermelstein, K.M. Merz, Y. Miao, G. Monard, C. Nguyen, H. Nguyen, I. Omelyan, A. Onufriev, F. Pan, R. Qi, D.R. Roe, A. Roitberg, C. Sagui, S. Schott-Verdugo, J. Shen, C.L. Simmerling, J. Smith, R. Salomon-Ferrer, J. Swails, R.C. Walker, J. Wang, H. Wei, R.M. Wolf, X. Wu, L. Xiao, D.M. York and P.A. Kollman *AMBER 2018*, University of California: San Francisco, 2018.
2. Martínez, L.; Andrade, R.; Birgin, E. G.; Martínez, J. M., PACKMOL: A package for building initial configurations for molecular dynamics simulations. *J. Comput. Chem.* ***30***, 2157-2164 (2009).
3. Wang, J.; Wolf, R. M.; Caldwell, J. W.; Kollman, P. A.; Case, D. A., Development and testing of a general amber force field. *J. Comput. Chem.* ***25***, 1157-1174 (2004).
4. Sprenger, K. G.; Jaeger, V. W.; Pfaendtner, J., The General AMBER Force Field (GAFF) Can Accurately Predict Thermodynamic and Transport Properties of Many Ionic Liquids. *J. Phys. Chem. B* ***119***, 5882-5895 (2015).
5. Darden, T.; York, D.; Pedersen, L., Particle mesh Ewald: An N·log(N) method for Ewald sums in large systems. *J. Chem. Phys.* ***98***, 10089-10092 (1993).
6. Ryckaert, J.-P.; Ciccotti, G.; Berendsen, H. J. C., Numerical integration of the cartesian equations of motion of a system with constraints: molecular dynamics of n-alkanes. *J. Comput. Phys.* ***23***, 327-341 (1977).
7. Berendsen, H. J. C.; Postma, J. P. M.; Gunsteren, W. F. v.; DiNola, A.; Haak, J. R., Molecular dynamics with coupling to an external bath. *J. Chem. Phys.* ***81***, 3684-3690 (1984).
8. Schrödinger, L. *Schrödinger Release 2017-1: Maestro*, Schrödinger, LLC: New York, NY, 2017.
9. Pettersen, E. F.; Goddard, T. D.; Huang, C. C.; Couch, G. S.; Greenblatt, D. M.; Meng, E. C.; Ferrin, T. E., UCSF Chimera—a visualization system for exploratory research and analysis. *J. Comput. Chem.* ***25***, 1605-1612 (2004).
10. Lynch, D. W., Diffusion and Ionic Conductivity in Cesium Bromide and Cesium Iodide. *Phys. Rev.* ***118***, 468-473 (1960).